

Planetary chaotic zone clearing: destinations and timescales

Sarah Morrison and Renu Malhotra

Lunar and Planetary Laboratory, The University of Arizona, Tucson, AZ 85721
morrison@lpl.arizona.edu, renu@lpl.arizona.edu

ABSTRACT

We investigate the orbital evolution of particles in a planet’s chaotic zone to determine their final destinations and their timescales of clearing. There are four possible final states of chaotic particles: collision with the planet, collision with the star, escape, or bounded but non-collision orbits. In our investigations, within the framework of the planar circular restricted three body problem for planet-star mass ratio μ in the range 10^{-9} to $10^{-1.5}$, we find no particles hitting the star. The relative frequencies of escape and collision with the planet are not scale-free, as they depend upon the size of the planet. For planet radius $R_p \geq 0.001R_H$ where R_H is the planet’s Hill radius, we find that most chaotic zone particles collide with the planet for $\mu \lesssim 10^{-5}$; particle scattering to large distances is significant only for higher mass planets. For fixed ratio R_p/R_H , the particle clearing timescale, T_{cl} , has a broken power-law dependence on μ . A shallower power-law, $T_{cl} \sim \mu^{-1/3}$, prevails at small μ where particles are cleared primarily by collisions with the planet; a steeper power law, $T_{cl} \sim \mu^{-3/2}$, prevails at larger μ where scattering dominates the particle loss. In the limit of vanishing planet radius, we find $T_{cl} \approx 0.024\mu^{-3/2}$. The interior and exterior boundaries of the annular zone in which chaotic particles are cleared are increasingly asymmetric about the planet’s orbit for larger planet masses; the inner boundary coincides well with the classical first order resonance overlap zone, $\Delta a_{cl,int} \simeq 1.2\mu^{0.28}a_p$; the outer boundary is better described by $\Delta a_{cl,ext} \simeq 1.7\mu^{0.31}a_p$, where a_p is the planet-star separation.

Subject headings: celestial mechanics — chaos — planet-disk interactions — planets and satellites: dynamical evolution and stability

1. Introduction

Dynamical chaos arising from the overlap of orbital resonances is responsible for orbital instabilities in the solar system (Lecar et al. 2001). For the simplest case of the planar circular restricted three body problem, the overlap of first order, $p : p + 1$, mean motion resonances occurs for $|p| > p_{ro} \gg 1$, where p is an integer,

$$p_{ro} \simeq 0.51\mu^{-\frac{2}{7}}, \quad (1)$$

and $\mu \ll 1$ is the planet-star mass ratio (Wisdom 1980). This resonance overlap condition defines an approximately annular “chaotic zone” in the vicinity of a planet’s circular orbit in which initially circular test particle orbits are rendered strongly chaotic. Making use of Kepler’s third law with Eq. 1, the half-width of this zone on either side of the planet’s orbit is given by

$$\Delta a_{ro} = c \mu^{\frac{2}{7}} a_p, \quad (2)$$

where a_p is the semi-major axis of the planet, and $c = 1.3$ is a numerical coefficient. An alternative analytical derivation by Malhotra (1998) found $c = 1.4$. A numerical analysis by Duncan et al. (1989) determined $c = 1.49$ for planet mass in the range $10^{-7} < \mu < 10^{-3}$. Although Eq. 2 was derived for a planet on a circular orbit, the relative insensitivity of Δa_{ro} to planet eccentricities up to about 0.3 (Quillen & Faber 2006) makes Eq. 2 a powerful tool for planetary dynamics. It is the first step in understanding the separations of long term stable planetary orbits in the solar system and in exo-solar systems. In our solar system, the outer edge of the asteroid belt and the inner edge of the Kuiper belt are approximately coincident with this estimate of the inner and outer boundaries of the chaotic zones of Jupiter and Neptune, respectively. For extra-solar planetary systems, this equation has been employed to constrain the locations of planetesimal belts in some systems (Moro-Martín et al. 2010; Schneider et al. 2014), and in estimating the masses of unseen planets that may be responsible for the observed gaps and edges of debris disks (Wyatt et al. 1999; Quillen 2006; Chiang et al. 2009; Su et al. 2013; Rodigas et al. 2014). Chiang et al. (2009) determined that Eq. 2, with a coefficient of $c = 2.0$, describes the cleared region of the Fomalhaut disk perturbed by an eccentric planet. Mustill & Wyatt (2012) and Deck et al. (2013) have studied the dependence of the chaotic zone on the test particles’ eccentricity, finding that non-zero initial eccentricities lead to wider chaotic zone widths.

In this paper, we answer the following questions: Where do chaotic zone particles go, and how long do they take to get there? A few previous studies have touched on these questions (e.g. Quillen (2006); Chiang et al. (2009); Bonsor et al. (2011); Deck et al. (2013); Frewen & Hansen (2014)), although none have attempted a systematic study. To this end, we investigate the orbital evolution of particles in initially circular orbits in a planet’s chaotic zone in the framework of the planar circular restricted three-body problem, for planet-star mass ratios in the range $10^{-9} < \mu < 10^{-1.5}$ (corresponding to Pluto-mass objects to brown dwarf mass objects orbiting solar mass stars). There are four possible final states of such particles: collision with the star, collision with the planet, escape to infinity, or bounded but non-collision orbits for infinite time. Using numerical integrations, we determine particle loss timescales from the chaotic zone and branching ratios for the particle final states as a function of planet mass and planet size. (As a practical matter, we determined the final states of particles at a finite but long time.) Although we refer to the massive bodies as “star” and “planet”, our results are applicable to other restricted three-body astronomical contexts with small mass ratios, such as binary minor planets, star/brown-dwarf, or black-hole/star systems. We describe our methodology in Section 2, and present our results in Section 3. We summarize and discuss an application of our results in Section 4.

2. Methodology

The test particle orbits of interest here are strongly chaotic and must be followed accurately through close planetary encounters. For the numerical integration of the equations of motion, we used the Bulirsch-Stoer method (Press et al. 1992) in the SWIFT integration package¹. This method utilizes a modified midpoint method for computing integration steps and an adaptive step size for controlling numerical error. We adopted a fractional truncation error tolerance of 10^{-10} . Throughout the integrations, we confirmed that there was no secular drift of the planet’s semi-major axis within 1 part in 10^{16} .

Within the framework of the planar circular restricted three-body problem, we adopt units such that the total mass (star and planet) is unity, the planet–star distance (a_p) is unity, and the orbital period of the planet about the star is 2π . We denote by μ the ratio of the planet mass to that of the host star. We carried out simulations for twelve values of $\log_{10} \mu$,

$$\log \mu = \{-9, -8, -7, -6, -5, -4.5, -4, -3.5, -3, -2.5, -2, -1.5\}.$$

For each of these cases, we integrated 7840 test particles in initially circular orbits (defined as osculating circular orbits about the star) in an annulus about the planet’s orbit.

For values of $\mu \leq 10^{-3}$, the initial test particle orbits were uniformly spaced within each of 98 annuli in the radial range $[a_p(1 - 1.95\mu^{2/7}), a_p(1 + 1.95\mu^{2/7})]$; this is approximately 30–50% larger than the resonance overlap zone defined by Eq. 2. In the cases of planet masses $\mu > 10^{-3}$, the half-width was extended out to $3.0\mu^{2/7}a_p$ in order to more effectively determine the extent of clearing. The initial longitude of the planet was zero and the initial angular positions of the test particles were chosen uniformly over the full range, $\{0, 2\pi\}$, with the exception that we excluded initial positions within $0.75R_H$ distance of the planet, where $R_H = (\mu/3)^{1/3}a_p$ is the planet’s Hill radius; the excluded region is approximately the region of stable satellite orbits in the restricted three body problem.

We integrated the test particle orbits for a time period of up to 10^8 revolutions of the planet to determine their final destinations and removal timescales. For most simulation results discussed here, integrations of 10^6 revolutions of the planet were sufficient. We stopped integrating a test particle under the following conditions:

1. *Particle’s periastron was within $0.01a_p$.* For $a_p = 1$ AU, this distance corresponds to approximately two solar radii. We adopted this distance as our definition for a collision with the star.
2. *Particle’s distance from the star exceeded $4a_p$.* We refer to this condition as ‘scattered’. Several test runs indicated that many of these particles would eventually travel to distances beyond

¹<http://www.boulder.swri.edu/~simshal/swift.html>

$100a_p$. This choice is additionally motivated by the observation that the planets in the solar system have separations of $(2-3)a_p$; multiple planet systems amongst the known exo-planets also typically have smaller separations (Fabrycky et al. 2012).

3. *Particle approached the planet within a prescribed small distance, R_p .* We refer to this condition as ‘collision with the planet’. We carried out three sets of simulations, one with $R_p = 0.1R_H$, the second with $R_p = 0.01R_H$ and the third with $R_p = 0.001R_H$.

Our choice of scaling the collision radius to the planet’s Hill radius is motivated by the expectation that the ratio of collisions to scatterings is governed by the square of the ratio of the surface escape velocity of the planet to the mean relative velocity of encounters, the so-called Safronov number, $\Theta = v_{esc}^2/v_{rel}^2$. For initially circular test particle orbits in the vicinity of the planet’s orbit, we expect that the typical relative velocity of encounter is on the order of the ‘Hill velocity’, $v_H = (\mu/3)^{1/3}v_p$, where v_p is the planet’s circular orbital velocity. In this case, Θ is inversely proportional to the ratio of the physical radius to the Hill radius of the planet,

$$\Theta = \frac{v_{esc}^2}{v_{rel}^2} \sim \frac{2Gm_p/R_p}{(\mu/3)^{2/3}Gm_*/a_p} = 6\frac{R_H}{R_p}. \quad (3)$$

The physical radius of a planet as a fraction of its Hill radius can be expressed as,

$$\frac{R_p}{R_H} = \left(\frac{3\rho_*}{\rho_p}\right)^{1/3} \frac{R_*}{a_p} = 0.0042 \left(\frac{\rho_* \rho_{\oplus}}{\rho_{\odot} \rho_p}\right)^{1/3} \frac{R_*}{R_{\odot}} \left(\frac{a_p}{1 \text{ AU}}\right)^{-1}, \quad (4)$$

where ρ_p, ρ_* are the mean density of the planet and star, respectively, ρ_{\oplus} is the mean density of Earth, R_* is the stellar radius, and ρ_{\odot} and R_{\odot} are the mean solar density and radius. This fraction is only weakly dependent on planet density, and is mainly dependent on planet-star separation. The currently known planets in the Galaxy have R_p/R_H concentrated in the range 0.01–0.1, as shown in Figure 1, since the majority of planets are discovered at small orbital radii by means of radial velocity and transit observations. The solar system planets have smaller values (also indicated in Figure 1), as do directly imaged planets, due to their greater distances from their host star.

Particles that did not meet the above conditions over the duration of the integrations are referred to as ‘survivors’.

We note that there is one known conserved quantity, the Jacobi integral (Hill 1878), that constrains the evolution of test particles in the circular restricted three body problem. For the planar case, the Jacobi integral is given by

$$J = -v^2 + 2(xy - \dot{x}y) + 2\left(\frac{\mu_1}{r_1} + \frac{\mu_2}{r_2}\right), \quad (5)$$

where $\mu_1 = (1 + \mu)^{-1}$, $\mu_2 = \mu(1 + \mu)^{-1}$, and r_1 and r_2 are the distances of the test particle from the star and the planet, respectively, and (x, y) and (\dot{x}, \dot{y}) are the particle’s position and velocity

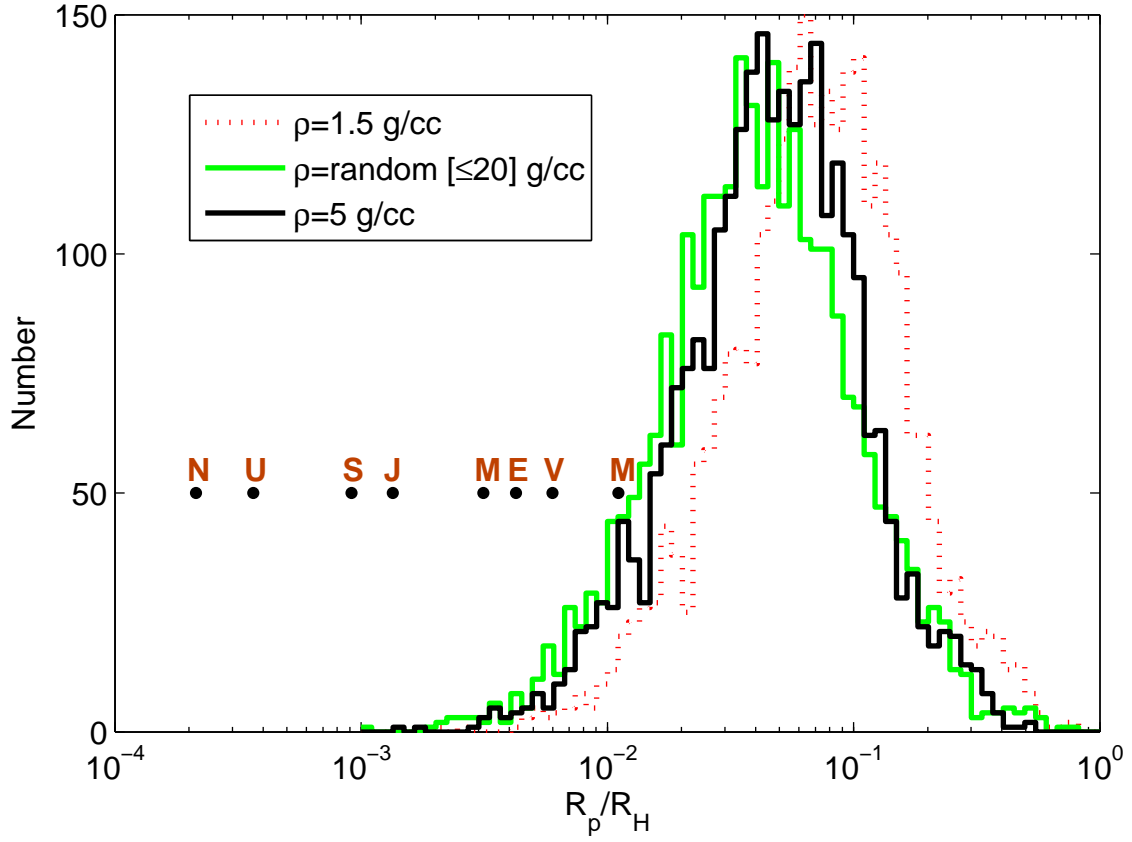


Fig. 1.— The distribution of R_p/R_H , the ratio of the physical radius of a planet as a fraction of its Hill radius. The histograms represent the distribution of *Kepler* planet candidates (radii from NASA Exoplanet Archive, retrieved on 06 March 2014) for different assumptions of bulk density. The black dots indicate the solar system planets.

vector in an inertial reference frame with origin at the barycenter of the star and the planet. A particle’s range in the x - y plane is bounded to regions where $\dot{x}^2 + \dot{y}^2 \geq 0$, therefore Eq. 5 (with $\dot{x} = \dot{y} = 0$, defines the boundary of this region, the so-called zero-velocity curve. It is pertinent to note that the zero-velocity curves for most of our initial conditions of particles within the chaotic zone allow all possible end-states, including collision with the star, collision with the planet, scatter to infinity, or possibly long-lived bounded orbits that may be either chaotic or quasi-periodic; i.e., the value of J alone is generally not indicative of the final destinations of our chaotic zone particles. A small minority of initial conditions, near the inner and outer edges of the chaotic zone annulus, have values of J that are bounded to remain entirely interior or entirely exterior to the planet’s orbit.

In addition to meeting the truncation error tolerance in the numerical integrations, we monitored the value of the Jacobi integral, J , for each test particle.

For the range of initial conditions of interest, J is close to 3, and $|J - 3|$ is small, on the order of $\mu^{4/7}$. We found that most of the chaotic zone test particles preserved their values of J to better than a part in 10^5 , but high numerical accuracy of the preservation of the Jacobi integral was sometimes more difficult to achieve than meeting the local truncation error tolerance. Unsurprisingly, the cases of small values of R_p/R_H pose a particularly stiff computational challenge. We identified numerical solutions as inaccurate if, over the course of the integrations, the fractional variation of J exceeded $2\mu^{4/7}/(3 + 2\mu^{4/7})$. Simulations with higher planet masses and lower values of R_p/R_H had larger numbers of these cases. For all cases of $R_p/R_H = 0.1, 0.01$ and $\mu \leq 10^{-2}$ that we simulated, we found that no more than 4% of our test particles failed this Jacobi conservation criterion; the case of $\mu = 10^{-4.5}$ for $R_p = 0.001R_H$ had the highest fraction, 27%, of the test particles failing our Jacobi conservation criterion. We found no obvious pattern in the initial conditions of these particles. These cases were excluded from the analysis that we report in the following sections. Discarding these cases has little effect on the reported results.

3. Results

3.1. Final destinations of chaotic zone particles

Overall, we find that particles do not hit the star in any of our simulations. Scattering to large distances is the most frequent outcome at larger planet masses; impact with the planet becomes relatively more frequent at larger planet sizes. We find that impact with the planet was the sole fate of non-surviving particles for planetary masses $\mu \lesssim 10^{-5}$ and $R_p/R_H \geq 0.001$. Scattering is the dominant loss mechanism when $\mu \gtrsim 10^{-3.5}$, 10^{-3} , and 10^{-2} , for $R_p/R_H = 0.001, 0.01$, and 0.1 , respectively. Figure 2 plots, as a function of μ , the fraction of non-surviving particles that were scattered or that collided with the planet, for each case of R_p/R_H .

The final destination of test particles as a function of initial semimajor axis and longitude are

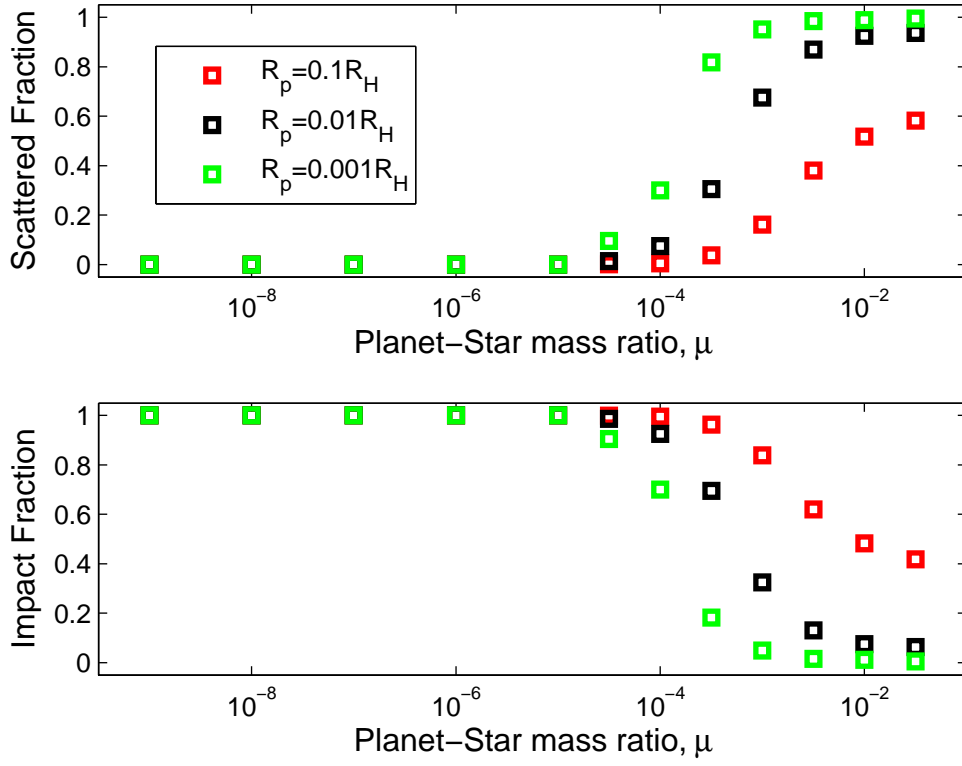


Fig. 2.— Fraction of non-surviving particles in the chaotic zone that are scattered (top) or impact the planet (bottom), as a function of μ , for fixed R_p/R_H .

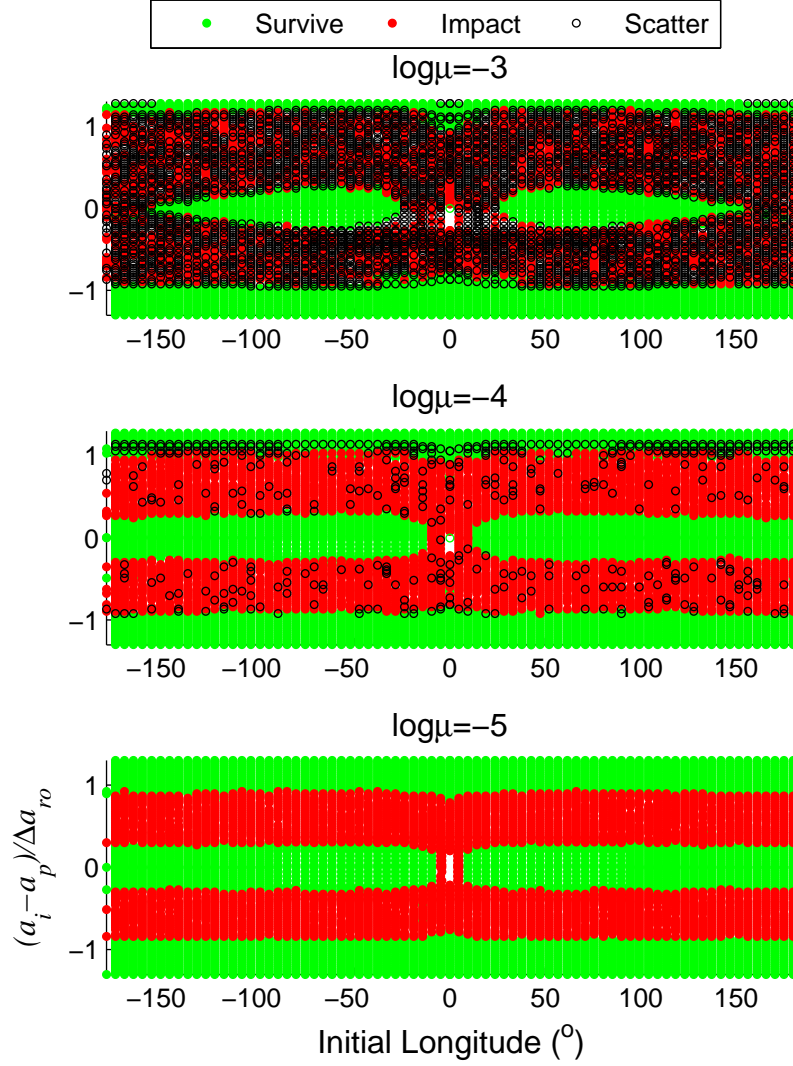


Fig. 3.— Final destination of chaotic zone particles as a function of particle initial conditions. Black points indicate scattering, red indicates impact with the planet, and green indicate survivors to the end of the simulation. We show results for three values of μ , for the case of $R_p = 0.01 R_H$. For clarity, we scale the initial semimajor axis separation from the planet, $a_i - a_p$, to the half-width of the chaotic zone, defined as $\Delta a_{ro} = 1.5 \mu^{2/7} a_p$. White patches indicate particles that were excluded due to poor conservation of the Jacobi constant.

shown in Figure 3, for three representative values of μ for the case of $R_p = 0.01R_H$. (Figures for all other simulated cases of μ and R_p/R_H are available by request from the authors.) We observe a noticeable asymmetry in Figure 3 (see also Figure 5) in the fates of the interior versus exterior particles with initial distance from the planet, especially for larger planet masses. The range of initial semimajor axis of particles that scatter or collide with the planet is smaller and closer to the planet’s orbit in the case of interior particles, and is relatively larger and extends farther from the planet’s orbit in the case of exterior particles.

In Figure 3, we also observe that most particles with initial orbits such that $|a_i - a_p| \lesssim R_H$ are survivors; a minor fraction of these collide with the planet. This surviving population is associated with the triangular Lagrange points, L_4 and L_5 . These particles are stable over the duration of our integrations, and survive in low eccentricity orbits ($e \ll 0.05$) either as Trojan-type orbits librating about L_4 or L_5 (analogous to the Trojan asteroids of Jupiter), or as “horseshoe” orbits librating about both L_4 and L_5 . For $10^{-9} \leq \mu \leq 10^{-4}$, we find that these “co-orbital” survivors span a radial range of 20 – 30% within the nominal chaotic zone annulus, $[a_p(1 - 1.5\mu^{\frac{2}{7}}), a_p(1 + 1.5\mu^{\frac{2}{7}})]$. Larger ranges of initial longitudes in the co-orbital region are stable for lower planet masses. The stable co-orbital region decreases significantly for planet masses $\mu > 10^{-4}$, and it vanishes for $\mu \geq 10^{-2}$. This behavior is likely related to the well known linear instability of the triangular Lagrange points, L_4 and L_5 , for $\mu \gtrsim 10^{-1.4}$ (Murray & Dermott 1999).

Survivors are also found near the outer edges of the chaotic zone. A few of these particles survive in nearly circular orbits, in libration in a first order mean motion resonance, and exhibit small ($< 1\%$) fractional changes in their semimajor axes. But, more typically, the survivors near the boundaries of the chaotic zone are found on eccentric orbits, with eccentricities up to ~ 0.6 . This population is larger for the chaotic zones of lower mass planets. For our smallest planet mass, $\mu = 10^{-9}$, the outer $\sim 45\%$ of the radial extent of the chaotic zone survives on eccentric orbits for more than 10^6 revolutions of the planet. However, these particles spend insignificant time in the “cleared zone” defined below.

3.2. Cleared zone

In previous studies, the boundaries of the chaotic zone have generally been defined in terms of the initial conditions. For practical astronomical applications (for example, gaps in protoplanetary or debris disks), it is of interest to define the extent of the “cleared zone”, the zone in which the density of surviving particles is nearly vanishing. In order to compute the radial boundaries of this zone, we adopted the following procedure. We first computed the time-averaged astro-centric distance of the surviving particles in their final osculating orbits, i.e., $\langle r \rangle = a_f(1 + \frac{1}{2}e_f^2)$. We binned these values into 98 bins in the range $a_p(1 - 1.95\mu^{\frac{2}{7}})$ to $a_p(1 + 1.95\mu^{\frac{2}{7}})$; these are the same bins that we adopted for the osculating semimajor axes of the test particle initial conditions. We computed the survivor fraction (the ratio of the number of survivors to the initial number) in each annular

bin. We then determined the interior and exterior boundaries of the cleared zone by finding the most distant annulus on either side of the planet that has a survivor fraction less than 5%. Figure 4 shows these inner and outer boundaries of the cleared zone as a function of μ , for the case of $R_p/R_H = 0.01$.

We observe a noticeable asymmetry in the interior and exterior cleared zones, which increases with increasing μ . For each case of R_p/R_H , we computed a least-squares fit to a power law of the form

$$\Delta a_{cl} = C \mu^\beta a_p, \quad (6)$$

to the interior and exterior boundaries of the cleared zone. The values of the parameters C and β are given in Table 1. We find, unsurprisingly, that both the power law index and the numerical coefficient have little dependence on the value of R_p/R_H . The cleared zone boundary interior to the planet’s orbit mimics the first order resonance overlap criterion, Eq. 2, with $c \simeq 1.2$. The exterior boundary has a slightly steeper power law index as well as a larger numerical coefficient; it is better described by $\Delta a_{cl,ext} = 1.7\mu^{0.31}a_p$. This asymmetry, which increases with increasing μ , arises because the locations and strengths of interior and exterior overlapping first order mean motion resonances are not symmetric.

Table 1: Best-fit power law function for the interior and exterior boundaries of the cleared zones.

R_p/R_H	Interior Boundary		Exterior Boundary	
	β	C	β	C
0.001	0.28±0.01	1.17±0.13	0.31±0.01	1.76±0.28
0.01	0.28±0.01	1.19±0.10	0.30±0.01	1.68±0.24
0.1	0.29±0.01	1.31±0.22	0.31±0.01	1.79±0.18

It is also interesting to examine the critical integer value, p_{ro} (Eq. 1), for which all $p : p + 1$ resonances having $|p| \geq p_{ro}$ are overlapping for a given value of μ . The nearest integer defined by Eq. 1 is indicated in Figure 4, adjacent to the values of μ investigated in our numerical simulations. We observe that for the larger values of μ , p_{ro} moves into the range of single digits. In this range, where the first order resonances are sparse, we can expect less smoothness in the relationship between Δa_{ro} and μ , as the overlap of neighboring resonances occurs at discrete intervals of μ . Indeed, for $\mu \gtrsim 10^{-2}$, we reach critical integer value $p_{ro} = 1$; this means that all possible first order mean motion resonances are overlapping. (We note that, formally, the assumption of $|p| \gg 1$ in the derivation of Eq. 1 fails for $\mu \gtrsim 10^{-3}$.) This could explain the diminished mass dependence on the size of the cleared zone for these mass ratios seen in Figure 4.

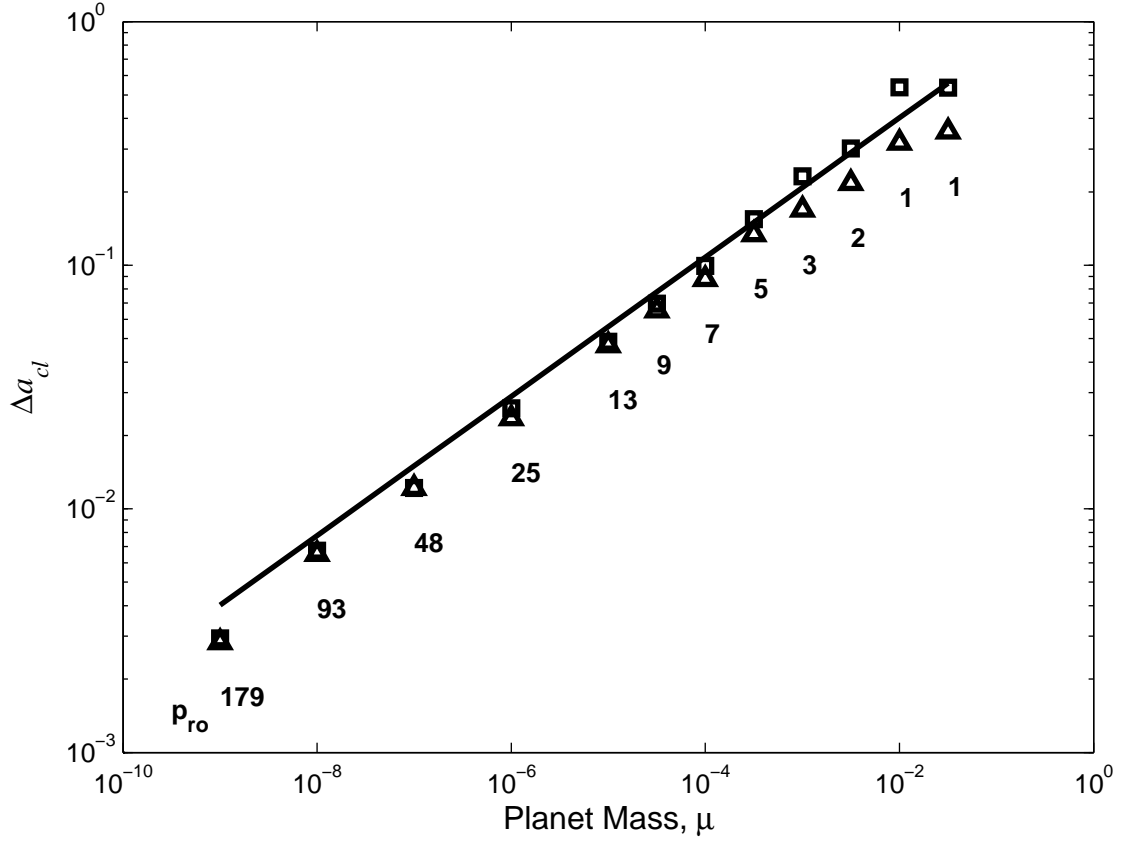


Fig. 4.— Interior (triangles) and exterior (squares) cleared regions, Δa_{cl} , for initially circular orbits near a planet with $R_p = 0.01R_H$. Numbers under each point correspond to the values of p_{ro} in Eq. 1, the analytical estimate of the most distant overlapping $p : p + 1$ resonance. The straight line indicates the chaotic zone width from the first order resonance overlap criterion (Eq. 2), with $c=1.5$.

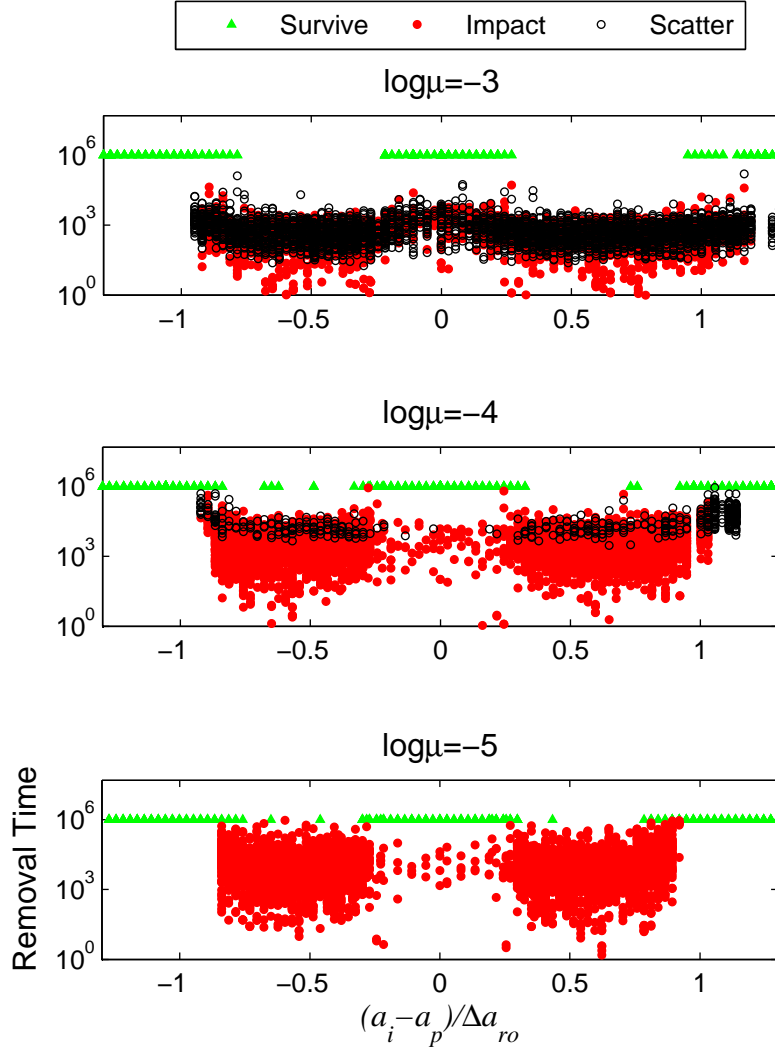


Fig. 5.— Removal time as a function of initial semimajor axis for three values of μ , for the case of $R_p = 0.01R_H$. Black points indicate test particles that were removed via scattering and red points indicate test particles removed via impact with the planet. Green points indicate survivors at the end of the simulation.

Table 2: Best-fit double power law models for the clearing timescale.

R_p/R_H	α_1	α_2	$\log_{10} T_b$	$\log_{10} \mu_b$
0.001	-0.35 ± 0.07	-1.59 ± 0.18	4.06 ± 0.36	-3.95 ± 0.38
0.01	-0.34 ± 0.05	-1.48 ± 0.19	3.10 ± 0.28	-3.43 ± 0.35
0.1	-0.37 ± 0.02	-1.48 ± 0.34	1.31 ± 0.19	-2.28 ± 0.27

Note. — T_b is given in units of the planet’s orbital period.

3.3. Clearing Timescales

The timescale for particles to be cleared from the chaotic zone generally decreases with increasing μ . There is also a noticeable difference in the time required to remove test particles via collision with the planet or via scattering. Figure 5 plots the removal time versus initial semimajor axis; the color of the points indicates the removal mechanism (scattering or collision with planet); the survivors are assigned a minimum lifetime equal to the duration of the simulation. As mentioned above, we find that particle removal via scattering to large distances occurs only for planet masses $\mu \geq 10^{-4.5}$, and it occurs throughout the chaotic zone. The scattered particles have longer removal times than those removed via collision with the planet. It is evident in Figure 5 that the range of initial conditions for which particles are cleared is asymmetric between the interior and exterior zones; however, their clearing timescales are similar.

The time evolution of the test particle population in the combined interior and exterior cleared zone is shown in Figure 6 for all the values of μ that we investigated, for the case of $R_p = 0.01R_H$. We plot the survivor fraction, the fraction that collide with the planet and the fraction that scatter, all as a function of time. We find that the ‘survivor’ fraction decays and eventually stabilizes to a final (non-zero) value over a characteristic time during which particles are lost to collision with the planet or to scattering. Figure 6 also shows that scattering is the dominant clearing mechanism for $\mu \geq 10^{-3}$; for lower planet masses, collision with the planet is the dominant clearing mechanism.

We can define a clearing timescale, T_{cl} , as the time required to reach 50% of the final survivor fraction within the cleared zone. These timescales are shown as a function of μ in Figure 7 for each of the three different cases of R_p/R_H . Clearing timescales become longer across the entire planetary mass range as the planet fills less of its Hill radius (lower R_p/R_H). We observe that, $T_{cl}(\mu)$ appears to have a broken power law shape, with a shallower slope at low masses compared to a steeper slope at high masses. The asymptotic slopes at high and low masses are similar for the three cases of R_p/R_H . The transition mass, μ_b , between the shallower and steeper slopes increases roughly linearly with R_p/R_H ; this transition mass approximately coincides with the transition between impact-dominated and scattering-dominated clearing of test particles.

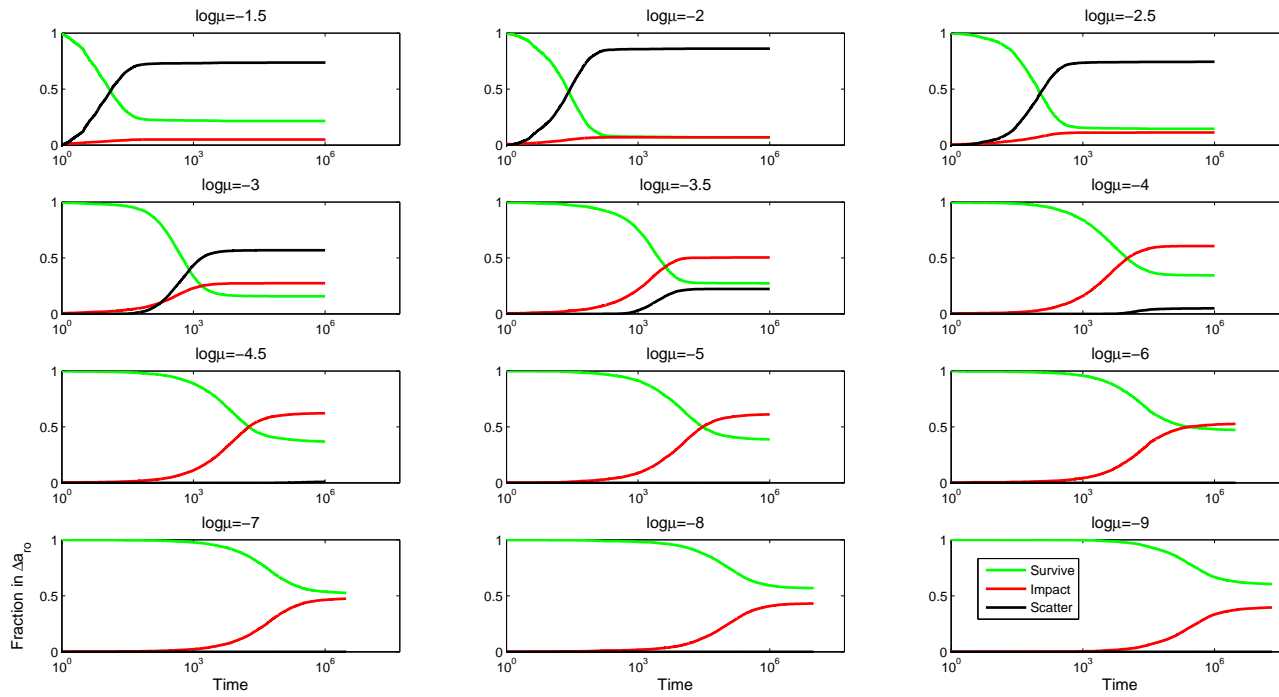


Fig. 6.— Time evolution of clearing within the chaotic zone, for planet masses ranging from $\mu = 10^{-9}$ to $10^{-1.5}$, for the case of $R_p = 0.01R_H$. Green lines indicate the survival fraction, red lines indicate the fraction of test particles that impact the planet, and black lines indicate the scattered fraction.

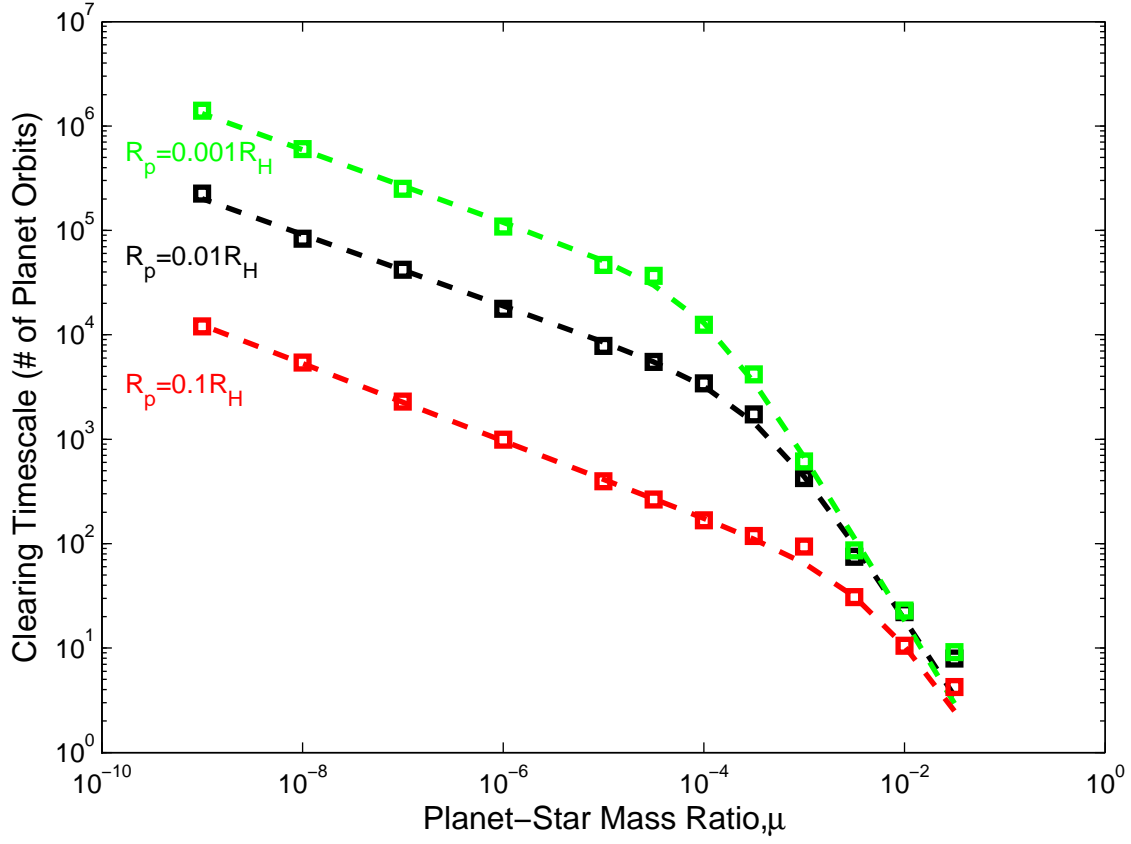


Fig. 7.— Clearing timescale (in units of the planet’s orbit period) as a function of planet mass, for the three cases of R_p/R_H . The best-fit double power law models (Eq. 7, Table 2) are shown as the dashed lines.

To describe the behavior of $T_{cl}(\mu)$, we computed a nonlinear least-squares fitting to a double power law function,

$$T_{cl}(\mu) = \frac{2T_b}{(\mu/\mu_b)^{-\alpha_1} + (\mu/\mu_b)^{-\alpha_2}}, \quad (7)$$

where α_1 and α_2 are the asymptotic power law slopes at $\mu \ll \mu_b$ and $\mu \gg \mu_b$, respectively, and T_b is the clearing timescale at the transition mass, μ_b . The best-fit values of the parameters T_b, μ_b, α_1 and α_2 , together with their 95% confidence limits, are listed in Table 2, for each of the three cases of $R_p/R_H = 0.001, 0.01, 0.1$. The best-fit double power law models are plotted as dashed lines in Figure 7.

4. Summary and Discussion

Using numerical integrations, we examined the orbital evolution of particles in the chaotic zone of a planet, within the framework of the circular, planar restricted three body model, in order to determine the final destinations of chaotic particles and their clearing timescales. Our results are summarized as follows.

1. For the planetary masses $\mu \lesssim 10^{-5}$ and planet sizes $R_p \geq 0.001R_H$, particles in initially circular orbits within the chaotic zone are lost via impact with the planet. For more massive planets, chaotic particles may either collide with the planet or scatter to large distances; scattering is the dominant fate of chaotic particles for planet-star mass ratios $\mu \gtrsim 10^{-3.5}$, 10^{-3} , and 10^{-2} , for $R_p/R_H = 0.001, 0.01, 0.1$, respectively. For the entire range of parameters that we investigated, we found no particles colliding with the star.
2. For planetary masses $10^{-9} \leq \mu \leq 10^{-4}$, most particles with initially circular orbits in the annulus of half-width approximately one Hill radius, $R_H = (\mu/3)^{\frac{1}{3}}a_p$, surrounding the planet’s orbit remain stable, in low eccentricity orbits in libration about the triangular Lagrange points, L_4 and L_5 . This stable “co-orbital” region is approximately 20–30% of the radial range defined by the classical chaotic zone annulus, Eq. 2. The stable co-orbital region decreases for $\mu > 10^{-4}$ and vanishes for $\mu \gtrsim 10^{-2}$.
3. Particles initially near the inner and outer boundaries of the chaotic zone can be long lived, surviving more than $\sim 10^6$ revolutions of the planet. A minor fraction survive on low eccentricity orbits in small pockets of stability associated with the libration centers of first order mean motion resonances. However, most of these particles survive in eccentric orbits and spend little time in the vicinity of the planet. This long-lived chaotic population is larger for lower mass planets; for $\mu = 10^{-9}$, nearly 45% of the outer radial extent of the chaotic zone survives in eccentric orbits for more than 10^6 revolutions of the planet.
4. The interior and exterior cleared zone boundaries, defined as the radius where the particle survivor fraction is reduced by more than 95%, are not symmetric about the planet’s orbit: the

outer cleared zone boundary is farther from the planet than the inner cleared zone boundary. The interior boundary mimics the classical first-order resonance overlap zone (Eq. 2), with a slightly smaller numerical coefficient, $c \simeq 1.2$. The exterior boundary of the cleared zone has a slightly steeper dependence on μ , and is better described by $\Delta a_{cl,ext} = 1.7\mu^{0.31}a_p$.

5. For fixed ratio of the planet radius to its Hill radius, the timescale, $T_{cl}(\mu)$, to clear the chaotic zone has double power law behavior (Fig. 7, Eq. 7, Table 2). A shallow slope prevails at small μ , a steeper slope at large μ . The asymptotic behavior is approximately $T_{cl} \propto \mu^{-\frac{1}{3}}$ for small μ and $T_{cl} \propto \mu^{-\frac{3}{2}}$ for large μ . The shallow slope behavior correlates with particle clearing dominated by collisions with the planet; the steeper slope behavior correlates with scattering being the dominant particle loss mechanism. For $R_p/R_H = 0.001$, the transition between the two power laws occurs at $\mu_b \approx 10^{-4}$; the corresponding clearing timescale is approximately 10^4 planet revolutions. The transition mass, μ_b , increases roughly linearly with R_p/R_H .

The lack of collisions with the star is rather surprising, at first sight. It may be due to a hidden dynamical constraint or may be owed to a computational limitation in our work. This is an interesting topic for a future investigation.

Our results show that collisions with the planet become less frequent while scattering becomes more frequent when the planet’s mass exceeds a critical mass, μ_b . The relative probabilities of particle loss by collision with the planet or by gravitational scattering are not scale-free, and μ_b depends upon the planet size. In our work, we scaled the planet size to its Hill radius, R_p/R_H , and computed the relative probabilities for values of this parameter spanning a fair range of physically relevant values. Smaller values of this parameter greatly challenge our computational resources. However, our results indicate that, for $R_p/R_H \rightarrow 0$, scattering is the dominant outcome. In this limit, the clearing timescale is nearly independent of R_p/R_H (as witnessed by the convergence at $\mu \gg \mu_b$ in Fig. 7). Using the results for $R_p = 0.001R_H$ as a proxy, the clearing timescale in the limit of vanishing R_p can be approximated as $T_{cl}(\mu) \approx 0.024_{-0.014}^{+0.032}\mu^{-\frac{3}{2}}$ (in units of the planet’s orbit period). Furthermore, in the parameter regime where clearing is dominated by collisions with the planet, the clearing timescale can be approximated as $T_{cl} \approx 1.33_{-0.20}^{+0.24}\mu^{-\frac{1}{3}}(R_p/R_H)^{-1} \approx a_p/R_p$. Thus, collisions dominate when $R_p \gg (11\mu)^{\frac{3}{2}}a_p$ for $\mu \ll 1$. We can summarize these estimates for the clearing timescale (in units of the planet’s orbital period) as follows,

$$T_{cl} \approx \begin{cases} 0.024\mu^{-\frac{3}{2}} & \text{if } R_p \rightarrow 0 \text{ (scattering dominated),} \\ \frac{a_p}{R_p} & \text{if } R_p \gg (11\mu)^{\frac{3}{2}}a_p, \mu \ll 1 \text{ (collision dominated).} \end{cases} \quad (8)$$

We remind the reader that these results are obtained for the planar case. The three dimensional case has two additional free parameters (inclination and nodal angles) and is computationally much more demanding: particle clearing timescales will, in general, be longer, and we can expect the collision dominated clearing time to scale as $\sim R_p^{-2}$. We hope to use the present results to develop intuition and to stimulate further numerical and theoretical analysis of this problem, so as to better understand the aggregate chaotic evolution of particles in the vicinity of a planet.

Despite their limitations, our results indicate that particle clearing timescales can be quite long in a planet’s chaotic zone, for all but the very massive close-in planets. Distant, high mass planets clear material predominantly by scattering rather than by collisions with the planet. To illustrate, Neptune would require more than ~ 20 Myr to clear its chaotic zone at its current semi-major axis (30 AU). Such long clearing timescales are pertinent for the interpretation of recent observations of debris disks of young exo-planetary systems. The clearing timescale for putative long period planets sculpting these disks can be comparable to the age of the system. Therefore, given the age of a system with a detectable gap in a circumstellar disk, the chaotic zone clearing timescale can be used to derive a lower mass limit of a (usually undetected) planet required to clear the gap.

HR 8799 and HD 95086 are two recently detected exo-planetary systems, each hosting a warm inner debris disk and a cold outer disk with inner edges beyond ~ 95 AU and ~ 63 AU, respectively (Su et al. 2009; Moór et al. 2013). A putative planet shepherding the inner edge of the cold disk would have orbital period ~ 750 yr and ~ 400 yr, respectively, and $R_p/R_H \lesssim 10^{-4}$. For the system ages of ~ 30 Myr and 17 Myr (Zuckerman et al. 2011; Pecaute et al. 2012), our results imply that a shepherding planet that could clear dust and planetesimals near the inner boundary of the cold disk must have a mass $\gtrsim 10M_\oplus$. (Our model uses massless disk particles and a fixed orbit of the planet; if the debris disk is massive, it could significantly affect the planet’s orbit, which may affect the robustness of this planet mass limit.) Indeed, HR 8799 is known to host four planets (directly imaged), each of 5–7 M_{Jup} (based on planetary thermal models); HD 95086 is known to host a single planet (directly imaged) interior to its cold debris disk, with an estimated mass of $5M_{Jup}$ also based on planetary thermal models (Marois et al. 2008, 2010; Rameau et al. 2013). The lower mass limit imposed by dynamical clearing timescales offers an independent constraint on the mass of directly imaged planets in debris disk systems; and it may be used to estimate the masses of undetected planets. This constraint may become of greater value in the future, when higher sensitivity and higher spatial resolution observations of exo-planetary systems hosting fainter debris disks sculpted by lower mass planets become available.

5. Acknowledgments

We thank Scott Tremaine and Roman Rafikov for helpful discussions. We also thank an anonymous reviewer for comments that have improved this manuscript. This research was partially supported by NASA (NESSF grant NNX13AO65H) and NSF (grant AST-1312498). This research made use of the NASA Astrophysics Data System Bibliographic Services and the NASA Exoplanet Archive.

REFERENCES

Bonsor, A., Mustill, A. J., & Wyatt, M. C. 2011, MNRAS, 414, 930

- Chiang, E., Kite, E., Kalas, P., Graham, J. R., & Clampin, M. 2009, *ApJ*, 693, 734
- Deck, K. M., Payne, M., & Holman, M. J. 2013, *ApJ*, 774, 129
- Duncan, M., Quinn, T., & Tremaine, S. 1989, *Icarus*, 82, 402
- Fabrycky, D. C., Lissauer, J. J., Ragozzine, D., et al. 2012, *ArXiv e-prints*
- Frewen, S. F. N., & Hansen, B. M. S. 2014, *MNRAS*, 439, 2442
- Hill, G. W. 1878, *American Journal of Mathematics*, 1, 5
- Lecar, M., Franklin, F. A., Holman, M. J., & Murray, N. J. 2001, *ARA&A*, 39, 581
- Malhotra, R. 1998, *Solar System Formation and Evolution: ASP Conference Series*, 149, 37
- Marois, C., Macintosh, B., Barman, T., et al. 2008, *Science*, 322, 1348
- Marois, C., Zuckerman, B., Konopacky, Q. M., Macintosh, B., & Barman, T. 2010, *Nature*, 468, 1080
- Moór, A., Ábrahám, P., Kóspál, Á., et al. 2013, *ApJ*, 775, L51
- Moro-Martín, A., Malhotra, R., Bryden, G., et al. 2010, *ApJ*, 717, 1123
- Murray, C. D., & Dermott, S. F. 1999, *Solar system dynamics*, 1st edn. (New York, New York: Cambridge University Press)
- Mustill, A. J., & Wyatt, M. C. 2012, *MNRAS*, 419, 3074
- Pecaut, M. J., Mamajek, E. E., & Bubar, E. J. 2012, *ApJ*, 746, 154
- Press, W. H., Teukolsky, S. A., Vetterling, W. T., & Flannery, B. P. 1992, *Numerical recipes in FORTRAN. The art of scientific computing*, 2nd edn. (Cambridge: University Press)
- Quillen, A. C. 2006, *MNRAS*, 372, L14
- Quillen, A. C., & Faber, P. 2006, *MNRAS*, 373, 1245
- Rameau, J., Chauvin, G., Lagrange, A.-M., et al. 2013, *ApJ*, 772, L15
- Rodigas, T. J., Malhotra, R., & Hinz, P. M. 2014, *ApJ*, 780, 65
- Schneider, G., Grady, C. A., Hines, D. C., et al. 2014, *ArXiv e-prints*
- Su, K. Y. L., Rieke, G. H., Stapelfeldt, K. R., et al. 2009, *ApJ*, 705, 314
- Su, K. Y. L., Rieke, G. H., Malhotra, R., et al. 2013, *ApJ*, 763, 118
- Wisdom, J. 1980, *AJ*, 85, 1122

Wyatt, M. C., Dermott, S. F., Telesco, C. M., et al. 1999, *ApJ*, 527, 918

Zuckerman, B., Rhee, J. H., Song, I., & Bessell, M. S. 2011, *ApJ*, 732, 61